Parametric image reconstruction using spectral analysis of PET projection data

Parametric image reconstruction using spectral analysis of PET projection data

Steven R Meikle†, Julian C Matthews, Vincent J Cunningham,
Dale L Bailey, Lefteris Livieratos, Terry Jones and Pat Price

MRC Cyclotron Unit, Hammersmith Hospital, Royal Postgraduate Medical School, Du Cane
Road, London W12 0NN, UK

Abstract. Spectral analysis is a general modelling approach that enables calculation
of parametric images from reconstructed tracer kinetic data independent of an assumed
compartmental structure. We investigated the validity of applying spectral analysis directly
to projection data motivated by the advantages that: (i) the number of reconstructions is reduced
by an order of magnitude and (ii) iterative reconstruction becomes practical which may improve
signal-to-noise ratio (SNR). A dynamic software phantom with typical 2-[^{11}C]thymidine kinetics
was used to compare projection-based and image-based methods and to assess bias–variance
trade-offs using iterative expectation maximization (EM) reconstruction. We found that the
two approaches are not exactly equivalent due to properties of the non-negative least-squares
algorithm. However, the differences are small (<5%) and mainly affect parameters related to
early and late time points on the impulse response function (K_1 and, to a lesser extent, VD).
The optimal number of EM iterations was 15–30 with up to a two-fold improvement in SNR
over filtered back projection. We conclude that projection-based spectral analysis with EM
reconstruction yields accurate parametric images with high SNR and has potential application
to a wide range of positron emission tomography ligands.

1. Introduction

Quantitative estimates of physiological parameters can be obtained from dynamic positron
emission tomography (PET) studies by relating the time course of labelled compound
to the tracer concentration in plasma via an appropriate tracer kinetic model. If the
model is sufficiently insensitive to noise, parameters can be estimated at the pixel level,
yielding so-called parametric or functional images. Conventionally, image reconstruction
and kinetic modelling are treated as separate estimation tasks with reconstruction of the full
dynamic sequence of images being performed prior to physiological parameter estimation.
Because of the large number of images to be reconstructed (typically 30 dynamic frames
multiplied by up to 50 axial slices), filtered back projection is usually preferred over iterative
reconstruction algorithms and, as a result, parametric images are often characterized by poor
signal-to-noise.

The tracer kinetic model can also be incorporated into the image reconstruction
process, treating the two processes as a single parameter estimation task. The expectation

---

† Present address: Department of PET and Nuclear Medicine, Royal Prince Alfred Hospital, Missenden Road,
Camperdown NSW 2050, Australia. E-mail address: steve@nucmed.rpa.cs.nsw.gov.au

maximization (EM) algorithm (Shepp and Vardi 1982, Lang and Carson 1984), for example, is easily extended to include a temporal component which may be described by a tracer kinetic model (Snyder 1984, Carson and Lange 1985, Matthews *et al* 1997). This approach has the potential to improve the noise characteristics of parametric images and is theoretically appealing as it unifies the tracer model and the imaging model and allows for more appropriate choice of weights in the optimization procedure. However, this approach has not been widely adopted as it remains computationally demanding. An alternative approach is to perform parameter estimation directly on the projection data prior to image reconstruction (Tsui and Budinger 1978, Huang *et al* 1982, Alpert *et al* 1984, Maguire *et al* 1996). This requires that the model can be expressed as a linear function of the unknown parameters. The advantages of this approach are that: (i) the number of reconstructions is reduced by an order of magnitude and (ii) as a consequence, iterative reconstruction of parametric images becomes practical which may lead to an improved signal-to-noise ratio (Wilson and Tsui 1993, Meikle *et al* 1994). However, the methods described to date are mainly restricted to specific models which are based on a compartmental description of the tracer kinetics. For example, the weighted integration technique assumes that all tissues in the field of view behave homogenously as a two-compartment system (Huang *et al* 1982, Alpert *et al* 1984, Carson *et al* 1986), although the method can also be extended to three-compartment models (Blomqvist 1984, Iida *et al* 1995). Further, the potential of iterative parametric image reconstruction has not been fully explored.

Our main interest is in the developmental tracers for oncology, particularly labelled anticancer drugs. In this important emerging application of PET (Price *et al* 1995, Wells *et al* 1996), as with other applications of new tracers, there is often insufficient *a priori* knowledge of the tracers' fate *in vivo* to construct a compartmental model, and parameter estimation is prone to bias if the model assumptions are incorrect. Therefore, we have explored spectral analysis, a more general modelling approach, which enables the determination of pharmacokinetic parameters with relatively few model assumptions (Cunningham and Jones 1993). The technique can be applied at a pixel level enabling calculation of parametric images independent of an assumed compartmental structure (Cunningham *et al* 1993). Therefore, it is applicable to a wide range of tracer studies. Furthermore, the model is linear and can, in theory, be applied equally well to projection data (Meikle *et al* 1996). If the validity of this approach can be demonstrated, spectral analysis has the advantage over other projection-based methods of employing a more general model which is particularly suitable for the study of developmental tracers. However, in the fitting procedure a non-negativity constraint is introduced which may result in spectral components representing very similar dynamics being merged. Hence, spectral analysis is not a linear operator and the validity of this approach is not immediately apparent.

In this study, we investigated the validity of applying spectral analysis to projection data. The trade-off between bias and variance when using iterative reconstruction of parametric images was also investigated, with comparison to filtered back projection. Finally, we have applied projection-based spectral analysis to a range of PET ligand studies and two examples are included to demonstrate potential applications of the technique.

2. Theory

In the spectral analysis method, the tissue time–activity curve x is modelled as a linear combination of basis functions, each of which is a single exponential in time convolved

with the arterial input function q:

$$x(t) = \sum_{k=1}^{N} q(t) \otimes \alpha_k \exp(-\beta_k t) \qquad \alpha_k \geqslant 0, \lambda \leqslant \beta_k \leqslant 1 \qquad (1)$$

where N is the maximum number of basis functions allowed in the model (typically 100) and λ is the decay constant of the radioisotope. The β values are fixed and are chosen to cover the spectrum of expected kinetic behaviour, from the slowest possible clearance (λ) to the fastest anticipated dynamic (e.g. 1 s^{-1}). x and q are not corrected for radioactive decay so that irreversible binding results in an apparent clearance of λ. Thus, the problem is to determine the values of α that best fit the measured data given predefined β values spaced logarithmically on the interval $[\lambda, 1]$. This can be written in matrix notation as

$$x = \mathbf{A}\alpha \qquad (2)$$

where x is the measurement vector, α is the solution vector, $\mathbf{A}$ is a $T \times N$ matrix (T is the number of time points) with elements:

$$A_{ij} = \frac{1}{t_{i+1} - t_i} \int_{t_i}^{t_{i+1}} q(t) \otimes \exp(-\beta_j t) \, dt \qquad (3)$$

and $t_i (i = 1, T)$ are the start and end frame times. Equation (2) can be solved for α using the non-negative least squares (NNLS) algorithm (Lawson and Hanson 1974) to minimize the following cost function:

$$\Phi(\hat{\alpha}) = (\mathbf{A}\hat{\alpha} - x)^T \mathbf{W}(\mathbf{A}\hat{\alpha} - x) \qquad \hat{\alpha} \geqslant 0 \qquad (4)$$

where $\mathbf{W}$ is a $T \times T$ matrix (usually diagonal) of suitably chosen weights. Typically, only a small number of non-zero α values are obtained in the solution vector, corresponding to the smallest number of exponentials that adequately describe the data. The fitted values of α, together with the corresponding chosen values of β, define the tissue unit impulse response function (IRF):

$$h(t) = \sum_{k=1}^{N} \hat{\alpha}_k \exp[-(\beta_k - \lambda)t] \qquad (5)$$

from which pharmacokinetic parameters can be calculated (see section 2.1 below). Now, the spectral analysis model (1) can be substituted into the time-dependent Radon transform:

$$y_i(t) = \sum_{j \in J} b_{ij} x_j(t) \qquad (6)$$

$$= \sum_{j \in J} b_{ij} \left(\sum_{k=1}^{N} q(t) \otimes \alpha_{jk} \exp(-\beta_k t) \right) \qquad (7)$$

where $y_i(t)$ is the number of counts recorded in projection bin i at time t, J is the subset of pixels that contribute to bin i, b_{ij} is the probability of a photon emitted from pixel j being recorded in bin i and $x_j(t)$ is the time–activity function corresponding to pixel j. Since the model is linear in the unknown coefficients (the α_k), parameter estimation can be performed either before or after back projection. Thus, the cost function of equation (4) can be rewritten for projection data as

$$\Phi(\hat{\alpha}) = (\mathbf{A}\hat{\alpha} - y)^T \mathbf{W}(\mathbf{A}\hat{\alpha} - y) \qquad \hat{\alpha} \geqslant 0 \qquad (8)$$

with the weights ($\mathbf{W}$) chosen to reflect the Poisson nature of noise in projection data (e.g. $w_{ii} = 1/\text{var}(y_i(t)) = 1/y_i(t)$). An alternative approach would be to substitute equation (7) into the cost function in place of $A\hat{\alpha}$. This would involve estimating α at the image

pixel level and forward projecting the model-predicted dynamic sequence of images for comparison with the measured projection data. This can be done within the framework of the EM algorithm, as discussed by Carson and Lange (1985) and more recently by Hudson and Walsh (1997) who also based their work on the spectral analysis method. A similar approach using a multi-exponential model was adopted by Haber *et al* (1996). These approaches are more computationally demanding as they require a forward projection step for each update of the parameter estimates. However, they have the advantage of providing direct estimates of the individual α values, rather than the overall IRF as in our method.

Fitting the model to projection data yields an estimate of the IRF for the heterogeneous mix of tissues lying along a given projection ray. This is equivalent to summing the IRF over all image pixels that contribute to bin i:

$$\hat{H}_i(t) = \sum_{j \in J} b_{ij} \hat{h}_j(t) \tag{9}$$

where $\hat{H}_i$ is the estimated IRF for projection bin i. Since equation (9) is in the general form of the Radon transform, it can be inverted using filtered back projection (FBP) or an iterative reconstruction technique to produce parametric images of the IRF ($\hat{h}$) at any specified time point. It should be noted that, although the model above is linear, the NNLS estimator is not, in general, a linear operator, i.e.

$$\hat{\alpha}_{\text{NNLS}}(\boldsymbol{x}_A + \boldsymbol{x}_B) \neq \hat{\alpha}_{\text{NNLS}}(\boldsymbol{x}_A) + \hat{\alpha}_{\text{NNLS}}(\boldsymbol{x}_B). \tag{10}$$

Indeed, NNLS is only linear for the special case where the best least-squares (unconstrained) solution contains positive values for all α_k.

2.1. Parameters of interest

Various kinetic parameters can be derived from the reconstructed IRF. In this paper, we refer to images of the IRF at 1 min, which is proportional to K_1, the product of blood flow and extraction ratio. Strictly, K_1 is defined as the IRF at time 0 but the intercept is very sensitive to measurement noise and may include a blood volume contribution as discussed by Cunningham *et al* (1993). Similarly, the IRF at a late time point (after reversible compartments reach steady state) is proportional to K_i, the irreversible disposal rate constant, for the case where irreversible binding occurs. Finally, we refer to images of the volume of distribution (VD) which is defined as the ratio of tissue to plasma concentration at steady state and is given by

$$\text{VD} = \int_0^\infty h(t)\, \mathrm{d}t = \sum_{k=1}^N \frac{\hat{\alpha}_k}{\beta_k - \lambda}. \tag{11}$$

In practice, estimates of VD are sensitive to errors in extrapolating the slow exponential components resulting in noisy parametric images, particularly for tracers that do not reach steady state within the duration of the PET study. In this study, we approximate VD by the integral from time 0 to T (the end of the scan), which provides a less noisy surrogate

$$\text{VD}_T = \int_0^T h(t)\, \mathrm{d}t = \sum_{k=1}^N \frac{\hat{\alpha}_k}{\beta_k - \lambda}(1 - \exp[-(\beta_k - \lambda)t]). \tag{12}$$

The ability of image-based spectral analysis to yield good-quality parametric images using parameters derived from the IRF has previously been demonstrated (Cunningham *et al* 1993, Tadokoro 1993). Such parameter estimates are less sensitive to measurement noise than

the individual α values, and yield images comparable to those obtained with conventional compartmental modelling and nonlinear least-squares fitting.

To summarize our method, the algorithm can be written as follows:

(1) Precompute basis functions (matrix **A**) by convolving measured arterial input function with predefined exponentials

(2) For each projection bin in turn:

(i) extract time-activity function, $y_i(t)$;

(ii) estimate coefficients (matrix α) by fitting spectral analysis model to $y_i(t)$ using NNLS;

(iii) form projection IRF ($\hat{H}(t)$) from estimated αs and predefined βs;

(iv) assign IRF value at specified time point to projection bin, e.g. $\hat{H}(t = 1 \text{ min}) \approx K_1$.

(3) Reconstruct parametric images from their projections.

In step 2(iv) above, estimates of VD_T can be obtained by summing the IRF according to equation (12) rather than choosing a specific time point.

3. Methods

3.1. Validation

To examine the validity of projection-based spectral analysis, a kinetic software phantom was constructed as follows. Typical 2-[^{11}C]thymidine (a marker of cell proliferation) kinetics for various tissues were derived from patient data ($n = 8$) acquired on an ECAT 931 whole body tomograph (CTI/Siemens, Knoxville, TN). The studies were acquired as dynamic scans for 60 min (see protocol below) following tracer administration while simultaneously measuring the tracer concentration in a radial artery catheter (Ranicar *et al* 1991) from which the input functions were obtained. Images were reconstructed using FBP with a Hann filter cut off at the Nyquist frequency ($f_{\text{nyq}} = 1.6 \text{ cm}^{-1}$) and time–activity curves (TACs) were calculated for regions of interest (ROIs) drawn over liver, spleen, skeletal muscle, bone, bone marrow and tumour. IRFs corresponding to these tissues were then determined by spectral analysis of the TACs. For each common tissue type, IRFs were averaged across subjects (by averaging spectral coefficients) and convolved with a typical arterial input function, resulting in typical TACs for each tissue (figure 1(*a*)). The TACs were divided into 30 discrete time intervals using a typical sampling schedule for 2-[^{11}C]thymidine (10×30 s, 5×60 s, 5×120 s, 5×180 s, 5×300 s). TAC values were then assigned to corresponding 'tissues' in a single slice of the Zubal phantom (Zubal *et al* 1994) which included a large (diameter about 3 cm) and a small (diameter about 1.5 cm) tumour (figure 1(*b*)). Dynamic projection data were simulated by forward projecting the image data into 3.13 mm bins on a 192×256 grid and reconstructed using FBP (Hann filter, $f_c = f_{\text{nyq}}$). Initially, no noise was added to either images or sinograms.

The spectral analysis fitting procedure was applied to the kinetic software phantom using both projection-based and image-based methods. In both cases, parametric images (or projections) of the IRF at 0, 1, 10, 30 and 60 min were calculated. Parametric projections were reconstructed using FBP and the same filter as for image-based spectral analysis (Hann, $f_c = f_{\text{nyq}}$). The two methods were compared by directly subtracting images obtained by image-based spectral analysis from those obtained by the projection-based method and by calculating the sum of squared residuals between the two sets of images. The experiment was repeated after adding Poisson noise to the sinograms typical of a
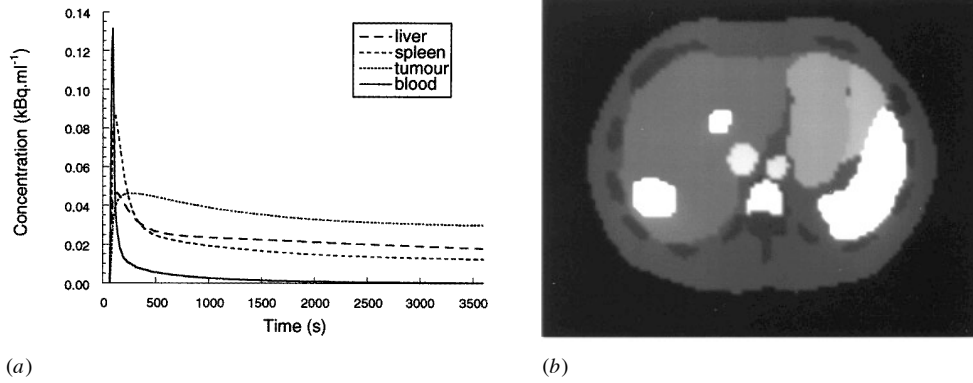
Figure 1. (*a*) Simulated 2-[^{11}C]thymidine kinetics for blood and three representative tissues: liver, spleen and tumour. (*b*) A slice of the digital Zubal phantom which includes a large (diameter $\approx$3 cm) and a small (diameter $\approx$1.5 cm) tumour.

2-[^{11}C]thymidine study acquired on an ECAT 931 scanner with septa extended (maximum count rate $\approx$25 kcounts/s).

3.2. Optimization of EM reconstruction

For the evaluation of EM reconstruction of parametric images, we chose two time points on the IRF: 1 min and 30 min, as well as the integral IRF from 0 to 60 min, VD_{60}, which approximates VD as discussed above. The 30 min time point was chosen to reflect irreversible uptake (K_i) of thymidine, allowing sufficient time for extracellular thymidine to equilibrate with plasma. Projections of these three parameters were calculated from the noisy sinogram data using projection-based spectral analysis and reconstructed using FBP (Hann filter, $f_c = f_{nyq}$) and from 1 to 64 iterations of the expectation maximization (EM) algorithm (Shepp and Vardi 1982). Accuracy of parameter estimation was evaluated by comparison with the known parameter values in ROIs defined on the original (noiseless) phantom for each tissue. Care was taken to avoid potential partial volume errors in the case of small structures such as the tumour and bone marrow. This analysis was performed on both FBP and EM images, in the latter case expressing bias as a function of iteration number. SNR in the tumours was also calculated as a function of iteration number, with the signal defined as the difference between tumour and background ROI means ($\bar{T}$ and $\bar{B}$ respectively) and the noise defined as the standard deviation in the background ROI ($\sigma(B)$), i.e.

$$ \text{SNR} = \frac{\bar{T} - \bar{B}}{\sigma(B)}. \tag{13} $$

We chose the background ROI to estimate noise rather than the tumour ROI because the size of the tumour would mean that estimates of standard deviation would be dominated by resolution effects instead of reflecting measurement noise. In the case of the 1 min IRF image where the tumour was not visualized, SNR was calculated as the ratio of the mean to the standard deviation in an ROI over the liver.
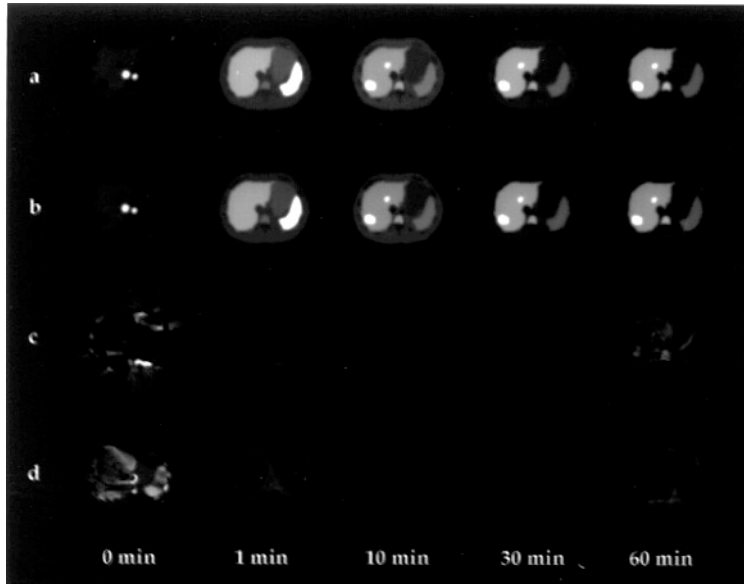
Figure 2. Parametric images of the noiseless software phantom corresponding to various times on the impulse response function as indicated. Rows a–d indicate: images calculated using projection-based spectral analysis followed by filtered back projection (a), images calculated using filtered back projection followed by image-based spectral analysis (b), relative differences between a and b (i.e. $(a - b)/b$) scaled to a maximum difference of 5% (c), the converse of c (i.e. $(b - a)/b$). In rows (c) and (d), negative values in the difference images were truncated to zero.

Table 1. Differences between estimated and known IRF images shown in figures 2 (without noise) and 3 (with noise).

Time (min)	Sum of squared residuals	
	Without noise	With noise
0	2.4×10^{-1}	5.9
1	2.5×10^{-6}	1.7×10^{-3}
10	4.6×10^{-8}	2.3×10^{-4}
30	1.9×10^{-7}	2.5×10^{-4}
60	1.4×10^{-6}	5.8×10^{-4}

3.3. Human studies

We have applied projection-based spectral analysis to a range of PET ligand studies acquired in 2D and 3D modes and present two such examples. The first example is a 2-[^{11}C]thymidine study performed on a 57-year-old female with metastatic carcinoma of the colon. The dynamic study was acquired with septa extended (2D) over 60 min (30 frames, 10×30 s, 5×60 s, 5×120 s, 5×180 s, 5×300 s) on an ECAT 931 scanner (CTI/Siemens, Knoxville, TN). After normalization and attenuation correction, projection-based spectral analysis was applied to the projection data and parametric images of VD_{60} and the IRF at 1 and 45 min were reconstructed using one iteration and 16 subsets of ordered subsets EM (Hudson and Larkin 1994) (OS-EM), which achieves equivalent convergence to 16 iterations of standard
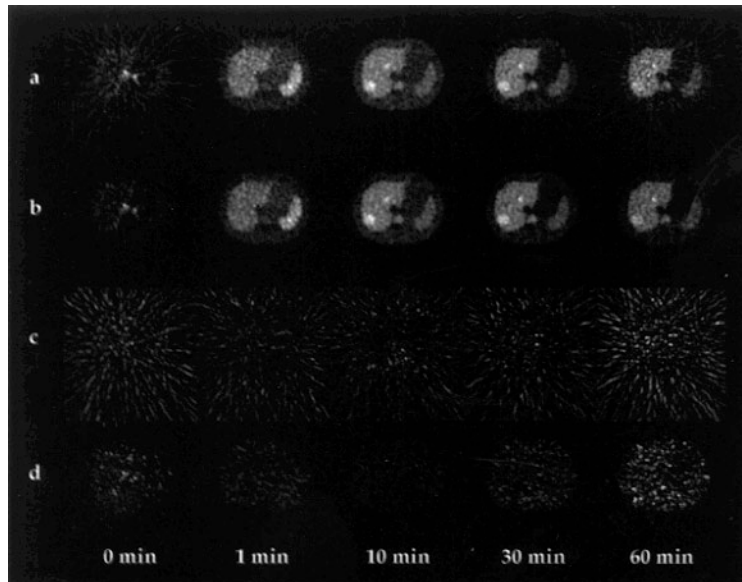
Figure 3. Parametric images of the noisy software phantom corresponding to various times on the impulse response function as indicated. The legend for rows a–d is the same as in figure 2 except that images in rows c and d are scaled to a maximum relative difference of 20%.

EM. Parametric images were also calculated using image-based spectral analysis following FBP reconstruction (Hann filter, $f_c = f_{nyq}$) of the dynamic data.

The second example is a study performed on a 59-year-old female with a high-grade astrocytoma, using a labelled anticancer agent, [^{11}C]temozolomide (Brown *et al* 1994). Temozolomide is an oral cytotoxic prodrug, i.e. it is initially non-toxic but degrades to a cytotoxic form under certain physiological conditions (which hopefully distinguish the tumour from normal tissues, resulting in targeted therapy). The reactive product of temozolomide is 5-(3-methyl)-1-triazenyl-1-yl)imidazole-4-carboxamide (MTIC), which is thought to achieve antitumour activity by methylating DNA guanine bases (Stevens *et al* 1987). The PET scan formed part of a study conducted in parallel with a phase II clinical trial by the UK Cancer Research Campaign. The dynamic study was acquired with septa retracted (3D) over 90 min (21 frames, 4×15 s, 2×30 s, 3×60 s, 7×300 s, 5×600 s) on an ECAT 953B scanner (CTI/Siemens, Knoxville, TN). The 3D sinograms were normalized, corrected for scatter (Bailey and Meikle 1994) and attenuation and rebinned into a 2D dataset using the single-slice approximation (Daube-Witherspoon and Muehllehner 1987). The same processing was applied to the rebinned sinograms as for the 2D study, except that the time point chosen for the 'K_i' image was 60 min.

4. Results

4.1. Validation

The subtraction images for noiseless data (figure 2) demonstrate that projection-based and image-based spectral analysis produce very similar results but the two techniques are not equivalent. The differences were <5% and were only appreciable at the extremes of the IRF (i.e. $t = 0$ and $t = 60$ min), particularly the zero intercept. The subtraction images
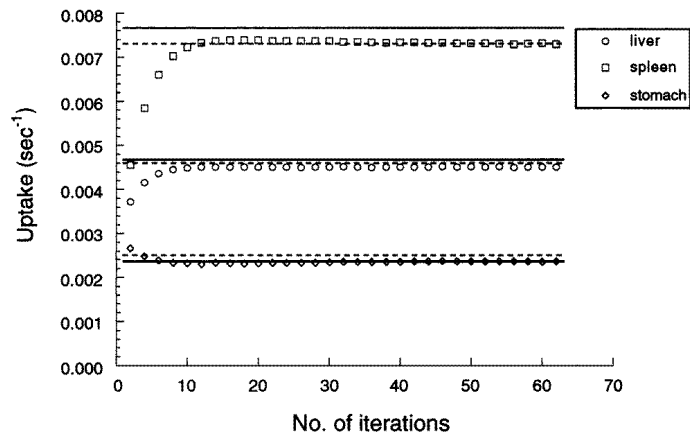
(a)
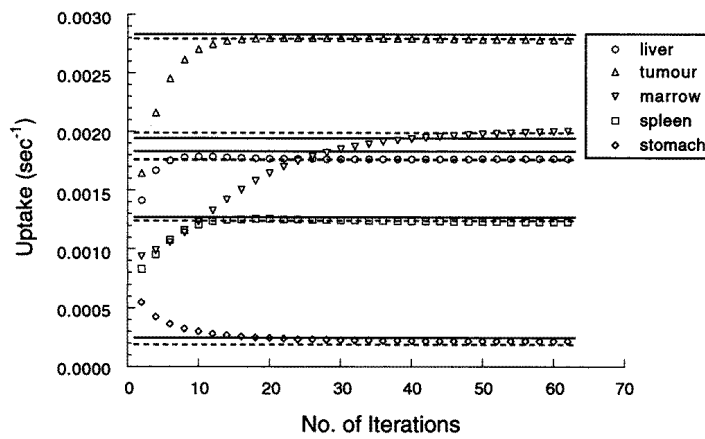
(b)
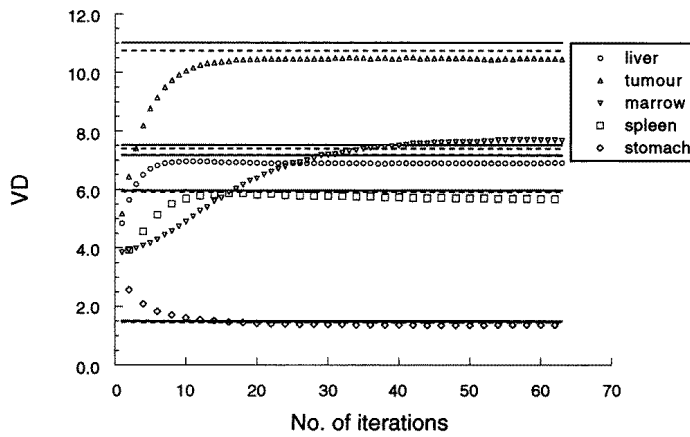
(c)

Figure 4. Estimates of the IRF at 1 min (*a*), the IRF at 30 min (*b*) and VD (*c*) in various tissues as a function of EM iteration number. Full lines indicate actual parameter values while broken lines indicate estimates obtained with filtered back projection.

for noisy data (figure 3) showed a similar trend but in this case the bias was dominated by noise. The impression given by the subtraction images is confirmed by the sum of squared residuals calculated as a function of time (table 1), which show that the differences are several orders of magnitude greater at $t = 0$ min than at other times ($t \geqslant 1$ min) and are somewhat higher at the end of the study ($t = 60$ min) than in the middle.

4.2. Optimization of EM reconstruction

Bias in parameter estimation with projection-based spectral analysis is shown in figure 4 as a function of EM iteration number. The method slightly underestimates K_1 (represented by the IRF at 1 min) (figure 4(*a*)) and VD (figure 4(*c*)) in regions with high parameter values (spleen in the case of K_1 and tumour in the case of VD) and the results are similar for FBP and EM. However, the agreement between estimated and actual values of the IRF at 30 min is very good (figure 4(*b*)). These results are consistent with those shown in figures 2 and 3 and table 1 since the parameters most affected by bias are those related to the extremes of the IRF (K_1 and, to a lesser extent, VD). EM values converged to the same values as FBP after 10–15 iterations in all regions except bone marrow which takes up to 50 iterations to converge. The SNR advantage of EM over FBP is apparent for all three parameters evaluated, as demonstrated in figure 5. For both the large and small tumour, EM produces higher SNR than FBP up to at least 40 iterations. These results suggest the optimal number of iterations (or ordered subsets) is 15–30, depending on the relative importance of bias versus SNR in a given application.

4.3. Human studies

Images of the IRF at 1 min, the IRF at 45 min and VD_{60} are shown for 2-[^{11}C]thymidine in figure 6. Note the relatively increased retention of [^{11}C]thymidine in the stomach (evident on K_i and VD_{60} images) which has higher proliferative index than the surrounding tissues. Similar images are shown for [^{11}C]temozolomide in figure 7, except that the image of specific retention is represented by the IRF at 60 min and VD is approximated by the integral IRF up to 90 min, VD_{90}. These images demonstrate higher extraction from blood of [^{11}C]temozolomide in the tumour rim (probably due to breakdown of the blood–brain barrier) compared with surrounding normal brain tissue, whereas retention is similar for tumour and normal brain. In both cases, the parametric images obtained using projection-based spectral analysis and OS-EM reconstruction are in good agreement with the conventional parametric images obtained with image-based spectral analysis and are appreciably less noisy.

5. Discussion

This study demonstrates the feasibility of applying spectral analysis directly to PET projection data and reconstructing parametric images with the iterative EM algorithm. We found that projection-based and image-based spectral analysis produce very similar results but the two techniques are not equivalent despite the linearity of the model. The differences mainly affect parameters related to early and late time points on the IRF (K_1 and, to a lesser extent, VD). When combined with iterative EM reconstruction, projection-based spectral analysis produces accurate parametric images with approximately two-fold improvement in signal-to-noise ratio over filtered back projection.
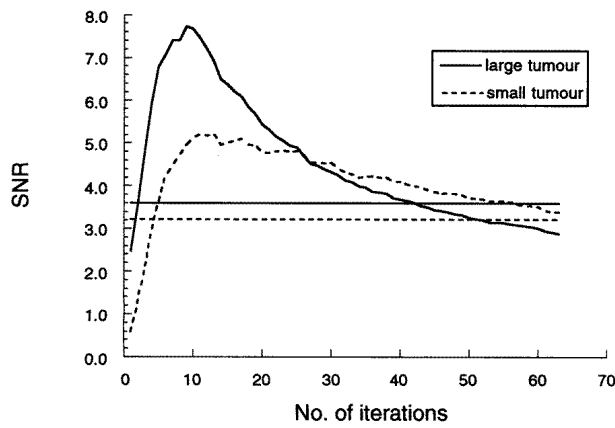
The differences observed between projection-based and image-based spectral analysis can be appreciated by examining the underlying model. For homogeneous image pixels the
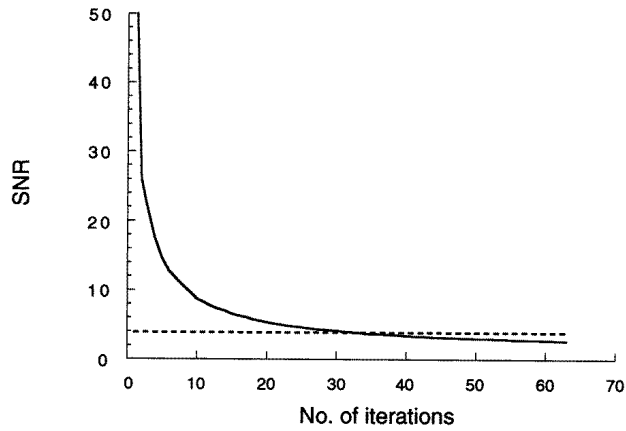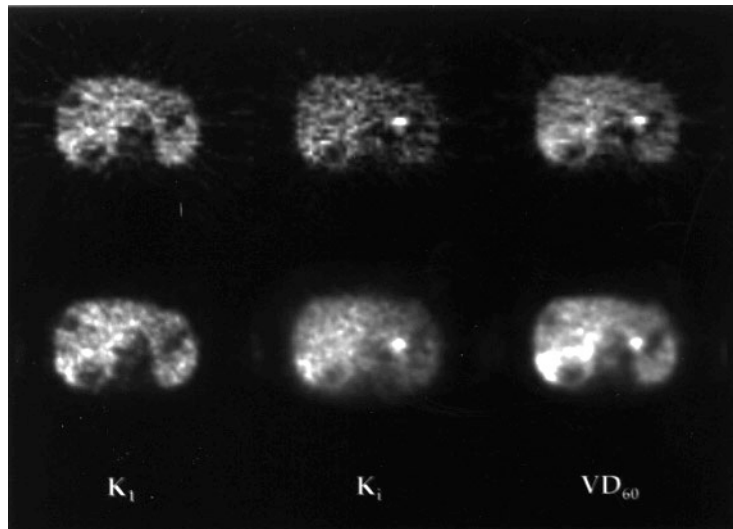
(*a*)
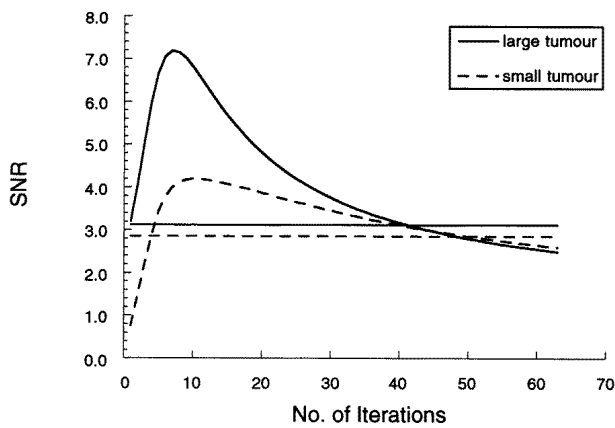
(*b*)

(*c*)

Figure 5. SNR for estimating the IRF in the liver at 1 min (*a*), the IRF in the two tumours at 30 min (*b*) and VD in the two tumours (*c*) as a function of EM iteration number. Horizontal lines indicate SNR obtained with filtered back projection.

Figure 6. Parametric images of the IRF at 1 min (K_1), the IRF at 30 min (K_i) and VD_{60} in a 2-[^{11}C]thymidine patient study acquired in 2D mode. Images in the first row were calculated using filtered back projection and image-based spectral analysis, while images in the second row were calculated using projection-based spectral analysis with OS-EM reconstruction.
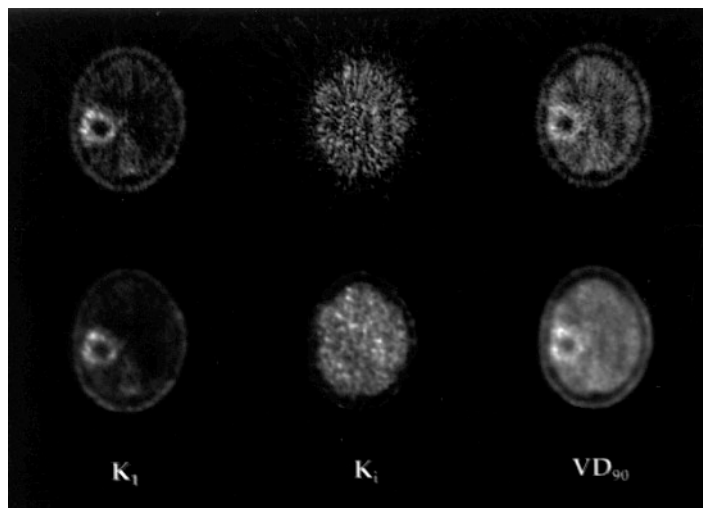
Figure 7. Parametric images of the IRF at 1 min (K_1), the IRF at 60 min (K_i) and VD_{90} in a [^{11}C]temozolomide patient study acquired in 3D mode. Images in the first row were calculated using filtered back projection and image-based spectral analysis, while images in the second row were calculated using projection-based spectral analysis with OS-EM reconstruction.

true underlying dynamics can be represented by a simple compartmental model, whose IRF is described by a positive sum of a small number (typically two or three) of exponentials. As long as the exponentials are sufficiently distinct and statistical noise is not too great, the IRF can be evaluated using spectral analysis. Conversely, the dynamics in the projection bin of a sinogram have contributions from a variety of tissues with diverse kinetics, making the IRF equal to a positive sum of many more exponentials than are typically found in an individual

image pixel. This heterogeneous IRF is just as appropriate to the spectral analysis model, as we have shown, but in practice it is more difficult to evaluate. For example, projection data are very noisy which results in a relatively flat error surface in the NNLS objective function. In these circumstances, the NNLS algorithm tends to merge adjacent coefficients in the solution vector. This is analogous to fitting an $(N-1)$-exponential to an N-exponential function, which causes undershoot at both ends. Hence, the multiple exponentials of the sinogram IRFs are approximated by fewer exponentials (typically three to five) resulting in an IRF which is close but not exactly equivalent to the true IRF. This is consistent with our observation that bias mainly affects the IRF at early and late time points, with the fast kinetics (early IRF values) poorly defined due to deficiencies of the input function and the slow kinetics (late IRF values) poorly defined due to the short duration of the scan and/or the short half-life of the isotope.

Despite these problems, the agreement between projection-based and image-based spectral analysis was very good. We believe this is because a good approximation of the true projection IRF can be obtained from the sum of just a few exponentials, despite the fact that individual α values and their corresponding βs may contain large errors. In future work, we will investigate factors that may influence and potentially reduce the bias, including the number and spacing of β values, the introduction of penalties into the NNLS objective function (Cunningham *et al* 1993, Chiao *et al* 1995) and the use of statistical or information criteria to further constrain the solution provided by NNLS (Cunningham *et al* 1998).

The spectral analysis technique is relatively insensitive to noise in the input function because of the convolution performed when calculating basis functions. However, as with image-based spectral analysis, it should be noted that biased parameter estimates may occur if the measured arterial input function is different to the actual input seen by the tissue of interest. For example, the administered bolus takes approximately 15 s longer to reach the sampling point at the radial artery catheter than it does to reach the tissue of interest, and is often somewhat more dispersed (Iida *et al* 1988). Although the time delay is small, it can cause problems in estimating fast dynamics and a poor fit to the early uptake phase of the time–activity curve. However, delay and dispersion can be accounted for in the model and have minimal impact on intermediate and slow dynamics which are often of greater interest. Further problems occur if the chosen input function does not accurately reflect the presence of labelled compounds that freely exchange with the tissue space and when significant concentrations of labelled metabolites contribute to the PET signal. It is important to note, however, that these problems are germane to most modelling techniques, including compartmental modelling, and are not unique to spectral analysis.

Performing parameter estimation directly on projection data has a considerable computational advantage over the traditional approach since the number of reconstructions is reduced from N dynamic frames per axial slice (where N is typically 20–30) to one image per parameter of interest. However, the computational advantage is offset by the fact that sinogram dimensions are typically larger than images (192×256 versus 128×128 on an ECAT 951R tomograph), thus requiring more model fits per slice (processing time is approximately 1 min per sinogram on a Sun Ultra 170 workstation). Taking these factors into account, the net saving with the projection-based approach is at least an order of magnitude. This time saving makes it practical to use iterative reconstruction methods and take advantage of their favourable noise properties (Wilson and Tsui 1993, Barrett *et al* 1994, Meikle *et al* 1994, Wilson *et al* 1994). We chose the EM algorithm in this work, with acceleration by the ordered subsets method, as it is widely used and well characterized. However, other iterative algorithms can also be used. Indeed, the EM algorithm is based on a Poisson noise model which does not apply when reconstructing physiological parameter

estimates (or randoms-corrected PET data for that matter). Therefore, with careful modelling of the noise distribution of parameter estimates, the penalized weighted least-squares algorithm (Fessler 1994) may be a better alternative. In future work, we will explore this and other alternative iterative reconstruction methods.

In this paper, we demonstrated clinical applications of the technique with two PET ligands, but the method is also applicable to single-photon emitters. The generality of the method arises from: (i) the spectral analysis model which makes no assumptions about the number or structure of tissue compartments, and (ii) the imaging model described by equation (7) which can accommodate both single-photon and coincidence geometries. Our method may be particularly useful in SPECT, as it overcomes one of the problems encountered with dynamic SPECT using rotating detectors. The problem arises when the tracer distribution changes appreciably during a given rotation (Juni 1992, Nakajima *et al* 1992). With conventional image-based modelling approaches this may cause image artefacts and biased parameter estimates, whereas with the projection-based approaches, physiological parameters (which are independent of time) are estimated directly on the projections and then reconstructed. Thus, such methods implicitly account for the fact that projections are acquired at different times. We recently confirmed that our approach will work in the dynamic SPECT setting using simulated ^{201}Tl-chloride kinetics (Meikle *et al* 1997). This work is ongoing. Further work is also required to examine the sensitivity of both the image-based and projection-based spectral analysis methods to the choice of sampling schedule, particularly in the case of rotating detector tomography.

6. Conclusions

Spectral analysis can be applied directly to PET projection data but, due to properties of the NNLS algorithm, the technique is not equivalent to the conventional approach of parameter estimation from reconstructed images. However, the differences are small ($<5\%$) and mainly affect parameters related to early and late time points on the IRF. For reconstructing parametric projections, 15–30 EM iterations (or ordered subsets) is optimal, with up to a two-fold increase in SNR. The technique has been applied to a range of PET ligand studies (both in 2D and 3D) and yields accurate parametric images with high SNR without imposing a compartmental model.

References

Alpert N M, Eriksson L, Chang J, Bergstrom M, Litton J E, Correia J A, Bohm C, Ackerman R H and Taveras J M
     1984 Strategy for the measurement of regional cerebral blood flow using short-lived tracers and emission
     tomography *J. Cereb. Blood Flow Metab.* **4** 28–34

Bailey D L and Meikle S R 1994 A convolution-subtraction scatter correction method for 3D PET *Phys. Med. Biol.* **39** 411–24

Barrett H H, Wilson D W and Tsui B M W 1994 Noise properties of the EM algorithm: I. Theory *Phys. Med. Biol.* **39** 833–46

Blomqvist G 1984 On the construction of functional maps in positron emission tomography *J. Cereb. Blood Flow Metab.* **4** 629–32

Brown G D, Turton D R, Luthra S K, Price P, Jones T, Stevens M F G, Baghurst D R, Mingos D M P, Osman S, Walters S L and Brady F 1994 Synthesis of [^{11}C-methyl]methylisocyanate and application with microwave heating to labelling the novel anticancer agent temozolomide *J. Label. Comp. Radiopharm.* **35** 100–2

Carson R E, Huang S C and Green M V 1986 Weighted integration method for local cerebral blood flow measurements with positron emission tomography *J. Cereb. Blood Flow Metab.* **6** 245–58

Carson R E and Lange K 1985 The EM parametric image reconstruction algorithm *J. Am. Statist. Assoc.* **80** 20–2

Chiao P, Fessler J A, Zasadny K R and Wahl R L 1995 Spectral analysis using regularized non-negative least-squares estimation *Conf. Record 1995 IEEE Medical Imaging Conf. (San Francisco)* (New York: IEEE) pp 1680–3

Cunningham V J, Ashburner J, Byrne H and Jones T 1993 Use of spectral analysis to obtain parametric images from dynamic PET studies *Quantification of Brain Function: Tracer Kinetics and Image Analysis in Brain PET* ed K Uemura, N A Lasson, T Jones and I Kanno (Amsterdam: Elsevier) pp 101–8

Cunningham V J, Gunn R N, Byrne H and Matthews J C 1998 Suppression of noise artifacts in spectral analysis of dynamic PET data *Quantitative Functional Brain Imaging with Positron Emission Tomography* ed R E Carson *et al* (San Diego, CA: Academic) at press

Cunningham V J and Jones T 1993 Spectral analysis of dynamic PET studies *J. Cereb. Blood Flow Metab.* **13** 15–23

Daube-Witherspoon M E and Muehllehner G 1987 Treatment of axial data in three-dimensional PET *J. Nucl. Med.* **28** 1717–24

Fessler J A 1994 Penalized weighted least-squares image reconstruction for positron emission tomography *IEEE Trans. Med. Imaging* **13** 290–300

Haber E, Oldenburg D, Farnocombe T and Celler A 1996 Quantitative dynamic SPECT tomography *Conf. Record 1996 IEEE Medical Imaging Conf. (Anaheim, CA)* (New York: IEEE) pp 1876–80

Huang S C, Carson R E and Phelps M E 1982 Measurement of local blood flow and distribution volume with short-lived isotopes: a general input technique *J. Cereb. Blood Flow Metab.* **2** 99–108

Hudson H M and Larkin R S 1994 Accelerated image reconstruction using ordered subsets of projection data *IEEE Trans. Med. Imaging* **13** 601–9

Hudson H M and Walsh C 1997 Density deconvolution using spectral mixture models *Proc. Computational Statistics and Data Analysis, IASC 2nd World Congress (Pasadena)* at press

Iida H, Bloomfield P M and Yamamoto S 1995 Effect of real-time calculation of functional images in clinical positron emission tomography *IEEE Trans. Med. Imaging* **14** 116

Iida H, Higano S, Tomura N, Shishido F, Kanno I, Miura S, Murakami M, Takahashi K, Sasaki H and Uemura K 1988 Evaluation of regional differences in tracer appearance time in cerebral tissues using [^{15}O]water and dynamic positron emission tomography *J. Cereb. Blood Flow Metabol.* **8** 285–8

Juni J E 1992 SPECT of rapidly cleared tracers: imaging a cheshire cat (editorial) *J. Nucl. Med.* **33** 1206–8

Lange K and Carson R 1984 EM reconstruction algorithms for emission and transmission tomography *J. Comput. Assist. Tomogr.* **8** 306–16

Lawson C L and Hanson R J 1974 *Solving Least Squares Problems* (Englewood Cliffs, NJ: Prentice-Hall)

Maguire R P, Calonder C and Leenders K L 1996 Patlak analysis applied to sinogram data *Quantification of Brain Function Using PET* ed R Myers, V Cunningham, D Bailey and T Jones (San Diego: Academic) pp 307–11

Matthews J C, Ashburner A, Bailey D, Harte R, Price P and Jones T 1997 The direct calculation of parametric images from dynamic PET data using maximum-likelihood iterative reconstruction *Phys. Med. Biol.* **42** 1155–73

Meikle S R, Eberl S, Matthews J C, Cunningham V J and Fulham M J 1997 Generalised parametric image reconstruction for dynamic emission tomography *J. Nucl. Med.* **38** 102P (abstract)

Meikle S R, Hutton B F, Bailey D L, Hooper P K and Fulham M J 1994 Accelerated EM reconstruction in total body PET: potential for improving tumour detectability *Phys. Med. Biol.* **39** 1689–704

Meikle S R, Matthews J, Cunningham V J, Bailey D L, Livieratos L, Jones T and Price P 1996 Spectral analysis of PET projection data *Conf. Record 1996 IEEE Medical Imaging Conf. (Anaheim, CA)* (New York: IEEE) 1888–92

Nakajima K, Shuke N, Taki J, Ichihara T, Motomura N, Bunko H and K H 1992 A simulation of dynamic SPECT using radiopharmaceuticals with rapid clearance *J. Nucl. Med.* **33** 1200–6

Price P, Harte R, Tilsley O, Matthews J, Brady F, Luthra S, Osman S, Babarovic R, Brown G, O'Reilly S, Brock C, Wells P and Jones T 1995 The use of radiolabelled anticancer drugs in phase I/II clinical trials and the assessment of therapeutic efficacy of new agents using PET *PET for Drug Development and Evaluation* ed D Comar (Dordrecht: Kluwer) pp 301–26

Ranicar A S O, Williams C W, Schnorr L, Clark J C, Rhodes C G, Bloomfield P M and Jones T 1991 The on-line monitoring of continuously withdrawn arterial blood during PET studies using a single BGO/photomultiplier assembly and non-stick tubing *Med. Prog. Through Technol.* **17** 259–64

Shepp L A and Vardi Y 1982 Maximum likelihood reconstruction for emission tomography *IEEE Trans. Med. Imaging* **1** 113–22

Snyder D L 1984 Parameter estimation for dynamic studies in emission-tomography systems having list-mode data *IEEE Trans. Nucl. Sci.* **31** 925–31

Stevens M F G, Hickman J A and Langdon S P 1987 Antitumour activity and pharmacokinetics in mice of 8-carbamoyl-3-methyl-imidazo [5,1-d]-1,2,3,5-tetrazin-4 (3H)-one (CCRG 91045; M&B 39831), a novel drug with potential as an alternative to dacarbazine *Cancer Res.* **47** 5846–52

Tadokoro 1993 *Quantification of Brain Function: Tracer Kinetics and Image Analysis in Brain PET* ed K Uemura, N A Lasson, T Jones and I Kanno (Amsterdam: Elsevier)

Tsui E and Budinger T F 1978 Transverse section imaging of mean clearance time *Phys. Med. Biol.* **23** 644–53

Wells P, Harte R J A and Price P 1996 Positron emission tomography: a new investigational area for cancer research *Clin. Oncol.* **8** 7–14

Wilson D W and Tsui B M W 1993 Noise properties of filtered-backprojection and ML-EM reconstructed emission tomographic images *IEEE Trans. Nucl. Sci.* **40** 1198–203

Wilson D W, Tsui B M W and Barrett H H 1994 Noise properties of the EM algorithm: II. Monte Carlo simulations *Phys. Med. Biol.* **39** 847–71

Zubal I G, Harrell C R, Smith E O, Rattner Z, Gindi G and Hoffer P B 1994 Computerized three-dimensional segmented human anatomy *Med. Phys.* **21** 299–302